Hindawi

Research Article

Synthesis, Characterization, and Evaluation of the Remediation Activity of *Cissus quadrangularis* Zinc Oxide Nanoparticle-Activated Carbon Composite on Dieldrin in Aqueous Solution

Calvince Ondijo ⑩,[1] Fredrick Kengara ⑩,[2] and Isaac K'Owino ⑩[3]

[1]*Department of Chemistry and Biochemistry, School of Sciences and Aerospace Studies, Moi University, P.O. Box 3900-30100, Eldoret, Kenya*
[2]*Department of Chemistry, School of Pure and Applied Sciences, Bomet University College, P.O. Box 701-20400, Bomet, Kenya*
[3]*Department of Chemistry, School of Natural Sciences, Masinde-Muliro University of Science and Technology, P.O. Box 190-50100, Kakamega, Kenya*

Correspondence should be addressed to Calvince Ondijo; makhondijo@gmail.com

In this study, zinc oxide-activated carbon nanocomposite was used as the adsorbent for the remediation of dieldrin in aqueous media. Zinc oxide nanoparticles (ZNPs) were synthesized from *Cissus quadrangularis* (*C. quadrangularis*) leaf extract, and activated carbon was derived from maize cobs. Nanocomposites were formulated by mixing the ZNPs with the activated carbon in a ratio of 1 : 50. The UV-Vis spectra showed a complete reduction of Zn^{2+} to Zn^0 with plasmon resonance bands in the range of 361–376 nm, which is a characteristic of ZNPs. The SEM images of ZNPs showed hexagonal-shaped particles of 15–20 nm, with face-centered cubic crystals, as demonstrated by XRD analysis. FTIR results showed absorption bands in the ranges 3500–3100 cm^{-1} (N-H stretch), 3400–2400 cm^{-1} (O-H stretch), 988–830 cm^{-1} (C-H bend), 1612 cm^{-1} (C=C stretch), 400–600 cm^{-1} (Zn-O stretch), and 1271 cm^{-1} (C-O bend). Batch adsorption experiments were performed using 20 ml of dieldrin solution at varying pH values (1–14), concentrations (5–100 ppm), temperatures (293–323 K), adsorbent dosages (0.01–0.12 g), and contact times (30–180 minutes) to determine the optimum conditions. The calculated thermodynamic parameters (ΔH°, ΔS°, and ΔG°) indicated that the adsorption was spontaneous and exothermic in nature, implying decreasing randomness of dieldrin molecules at the solid-liquid interface. The isotherm and adsorption kinetics for the composite showed that the absorption process followed Langmuir isotherm and pseudo-second-order kinetics. Adsorption capacities of the nanoparticles, activated carbon, and nanocomposite at a reaction time of 120 minutes and pH of 7 were 3.72 ± 0.068 mg/g, 3.92 ± 0.061 mg/g, and 4.0 ± 0.102 mg/g, respectively, with corresponding percentage removals of 93.12 ± 0.044, 98.04 ± 0.044, and 99.76 ± 0.332. Thus, the nanocomposite exhibited a better sorbing potential for dieldrin in solution than activated carbon. This study recommends testing the remediation potential of the synthesized nanocomposite on other persistent organic pollutants.

1. Introduction

In recent years, environmental pollution of water resources with organochlorine compounds such as DDT (dichloro-diphenyl-trichloroethane), aldrin, dieldrin, lindane, methoxychlor, endosulfan, and hexachlorobenzene has been widely reported [1]. These organochlorines have been classified as persistent organic pollutants (POPs) due to their tendency to remain intact in the environment for long periods. They accumulate in the fatty tissue of living organisms and are toxic to humans and wildlife, especially as endocrine disruptors [2]. Aldrin and dieldrin have been used against insects that cause damage to timber, corn, rubber in telecommunication cables, plywood, and building boards [3]. People get exposed to dieldrin when drinking contaminated water and eating fish and meat of animals in a

contaminated ecosystem [4]. Long-term exposure to dieldrin poses serious health risks associated with mutagenic and carcinogenic effects in humans [1]. This has led to the search of effective and economical techniques for removing dieldrin from water sources.

Dieldrin has been removed from the environment using adsorption with various adsorbents. Examples include unconsolidated aquifer sands [5] and triolein-embedded composite adsorbent [6]. Others include parent and processed montmorillonite clays [7], commercial activated carbon [8], and graphene oxide-magnetic nanoparticles [9]. Ramya et al. remediated dieldrin in the presence of sunlight using titanium dioxide nanoparticles as a catalyst. On the other hand, activated carbon-zinc oxide nanocomposite was used as a photocatalyst for the reduction of Cr(VI) under visible light irradiation [10]. The nanocomposite has also been used in the removal of celestin blue B (CBB) dye from simulated textile wastewaters [11] and high-performance supercapacitor electrodes and catalysts [12, 13]. Dieldrin has also been remediated with various agricultural wastes. Examples include polymeric resins [14] and cashew nut shells [15]. Others included wood, bagasse pith, maize cobs, and rice hull ash [15].

Attention has been drawn to zinc oxide nanoparticles (ZNPs) because of their exceptional physicochemical properties [16]. ZNPs among other nanoparticles have recently attracted much interest because of their unique qualities such as high catalytic and photochemical activities [17]. Zinc oxide nanoparticles impregnated with pea peels have also been used in the sorption of chlorpyrifos [18]. Powdered activated carbon derived from pomegranate peel extracts coated onto zinc oxide nanoparticles have also been applied for the removal of cephalexin. Lastly, the composite of ZnO nanoparticles and biomass-based activated carbon has been used in the remediation of methylene blue in wastewater [19] and rhodamine B in water under ultraviolet (UV) irradiation [20]. It is believed that better results can be attained by using activated carbon as a support for nanoparticles due to its high abundance, economical value, expansive surface area, reusability, and unique chemical properties such as its surface has a large volume of pores [21]. Activated carbon has good adsorption capability due its internal structure consisting of a large number of fine pores that act as surfaces for adsorption [10]. Therefore, a composite of ZNP-activated carbon could make a good sorbent for removing pollutants from contaminated media.

In this study, a composite of ZNP-activated carbon derived from agricultural-based waste was used as the adsorbent for the adsorption of dieldrin in aqueous media. Adsorption technology utilizing agricultural waste amended with nanoparticles has been used for inexpensive treatment of organic pollutants in the environment [22]; nanoparticles amended with activated carbon have not been used for the remediation of dieldrin. In particular, the effect of zinc oxide amended with activated carbon derived from maize cobs on the adsorption of dieldrin in aqueous media has not been tested. Therefore, there is lack of knowledge on whether application of the method would result in the removal and remediation of dieldrin through degradation, hence necessitating this study.

In this study, ZNPs were synthesized using green approaches other than physical and chemical methods which are uneconomical due to high amounts of wastes generated, high energy input, and low yield of nanoparticles after synthesis [23]. The natural extracted plant material used in the synthesis of the nanoparticles contain some phytochemicals acting as reducing, stabilization, or capping agents in the synthesis process [17]. Most researchers have now focused on formulation of activated carbon as a support for nanoparticle sorbents due to its high abundance, economical value, expansive surface area, reusability, and unique chemical properties such as its surface has a large volume of pores [24]. Plants are preferred in the synthesis of nanoparticles because of their exclusive phytochemical content [25]. According to literature review, *C. quadrangularis* species contain various phytochemicals acting as a capping and stabilizing agent in the synthesis of nanomaterials [26, 27]. *C. quadrangularis* leaf extracts can hence be used in reducing and capping of salt solutions. The objectives of the study were as follows: (i) synthesis of zinc oxide nanoparticles using *C. quadrangularis* leaf extract and their characterization using a particle analyzer and FTIR, SEM, XRD, and UV-Vis spectrometry; (ii) formulation of activated carbon from maize cobs as a support for ZnO loading and its characterization using a particle analyzer and FTIR, SEM, and XRD analysis; (iii) determining the impact of effective parameters, i.e., pH, adsorbent dose, temperature, initial concentration, and contact time on dieldrin removal efficiency; (iv) modelling the adsorption equilibrium and kinetics to examine the adsorption behavior of dieldrin onto AC-ZnO nanoparticles; and (v) determining the adsorption mechanism of dieldrin onto the AC-ZnO nanocomposite.

2. Materials and Methods

2.1. Chemicals and Reagents. The chemicals and reagents used in the research were zinc nitrate, potassium iodide, bromine water, lead acetate, sodium hydroxide, potassium hydroxide, distilled water, ferric chloride, hydrochloric acid, mercuric chloride, magnesium metal, chloroform, analytical aluminum chloride, hexane, silica gel, diethyl ether, copper turnings, acetone, anhydrous sodium sulphate, ammonium sulphate, copper sulphate, absolute methanol (99.9%), absolute ethanol (99.9%), sulphuric acid, and dieldrin standard (≥95%). The reagents and standards were all of analytical grade supplied by Sigma-Aldrich (USA). The apparatus and analytical instruments used in this study were weighing balance, centrifuge, heater, magnetic stirrer, UV-visible spectrophotometer (Shimadzu UV1860, Japan), Fourier transform infrared microscope (FTIR JASCO 4100, USA), mobile Hydrolab Quanta, scanning electron microscope (Hitachi S3000N, Germany), X-ray diffraction spectrometer (PANalytical X'Pert Pro, Netherlands), blender, ice box, ultrapure water, crucible, furnace, weighing balance oven, and water bath.

2.2. Sample Collection and Preparation. Fresh *Cissus quadrangularis* leaves were harvested from plants grown in their natural habitat in Kisumu East sublocation, Kisumu County, Kenya ($0°06'2''$ S, $34°46'59.4''$ E). They were identified and authenticated at the Department of Biological Sciences, Masinde Muliro University of Science and Technology (Kenya); whereas maize cobs were randomly collected from Kango sublocation, Kisumu County, Kenya ($0°05'31.7''$ S, $34°54'42.1''$ E). The collected leaves were cleaned by washing with running tap water followed by rinsing with double-distilled water. The cleaned leaves were then dried under the shade for 3 weeks. The dried material was ground into fine powder in an electric blender, and the powder was stored in desiccators awaiting extraction. Extraction was done by weighing out 1 g of powder and then adding 50 ml of methanol to it in a Soxhlet extractor for 48 hours at 60°C. All the extracts were filtered through Whatman No. 1 paper, and the collected filtrate was evaporated to 10 ml using a rotary evaporator [28]

2.3. Phytochemical Screening of C. quadrangularis. The extracts were subjected to phytochemical screening to test for the presence of alkaloids, saponins, phenols, tannins, anthraquinones, terpenes, flavonoids, proteins, steroids, and glycosides, following standard procedures as reported by Dhanasekaran [29].

2.4. Synthesis of ZNPs. Measured 50 ml of *C. quadrangularis* leaf extract was transferred into a conical flask and heated to 60°C on a hot plate [30]. Then, 5 g of zinc nitrate was added to the solution. The mixture was heated until the suspension turned deep yellow in color [31]. The yellow paste was then poured into a ceramic crucible, transferred into a furnace, and heated at 400°C for 2 hr. A light white-colored solid of zinc oxide was collected, dried, crushed, and pulverized to obtain the powdered form of zinc oxide nanoparticles [31].

2.5. Synthesis of Activated Carbon Derived from Maize Cobs. The maize cobs were washed with running tap water and double-distilled water to remove adhering dust [32], dried at 105°C in an oven for 4 hr, and then crushed into particles using a mortar and pestle. Accurately weighed samples of the dried maize cob particles were carbonized by heating at 400°C in limited air in a furnace for 1 hour. The biochar derived from maize cobs was then mixed with solid KOH at a ratio of 1 : 1 (wt/wt). The biochar was then activated by heating at 600°C in limited air for 1 hr in a furnace [33]. The activated carbon was then washed with 0.5 M HCl and deionized water until a rinse pH of 7 was achieved.

2.6. Synthesis of Zinc Oxide Nanoparticle-Activated Carbon Nanocomposite. Measured 0.10 g of zinc oxide nanoparticle was mixed with 200 ml of ultrapure water, followed by agitation for 10 min using a magnetic stirrer to obtain a uniformly distributed mixture. Thereafter, 5 g of the maize cobs-derived activated carbon was then added to the solution and placed in a magnetic stirrer at 500 rpm for 10 hr to complete the coating process. The filtrate was washed with ultrapure water and then dried in an oven at 95°C for 10 hr to obtain the zinc oxide-activated carbon nanocomposite [13].

2.7. Characterization of the ZNPs, Activated Carbon, and Nanocomposite. The synthesized ZNPs, activated carbon, and the nanocomposite were characterized using a UV-visible spectrophotometer (Shimadzu UV1860, Japan), Fourier transform infrared microscope (FTIR JASCO 4100, USA), scanning electron microscope (Hitachi S3000N, Germany), particle size analysis (Nanotrac MRB, USA), and X-ray diffraction spectrometer (PANalytical X'Pert Pro, Netherlands). The synthesized ZNPs were monitored by UV-Vis spectrometry within the range of 200 nm–800 nm (Shimadzu UV 1860, Japan). FTIR spectrum analysis was used to detect the functional groups present on the adsorbent. The size of the synthesized sorbents was assessed using a particle analyzer and confirmed with the XRD patterns. The surface morphology and size distribution of the synthesized nanocomposite were assessed using SEM.

2.7.1. FTIR Characterization. The solution containing the nanoparticle, activated carbon, and nanocomposite was centrifuged at 14000 rpm for 10 min to remove any residue that was not the capping agent, and the supernatant liquid was discarded. The resulting suspension was then redispersed and oven-dried to a dry powder, which was then mixed and pulverized with potassium bromide. The mixture was pressed in a mechanical press to form a thin pellet, which was put in a sample holder for FTIR analysis to obtain a spectrum.

2.7.2. UV-Vis Characterization. The ZNPs were dispersed in 3 ml methanol, and then the solution was subjected to UV-Vis spectroscopy over a scan range of 200 nm to 800 nm. Suspensions of ZNPs in methanol were measured at different aging times at room temperature.

2.7.3. SEM Characterization. For SEM analysis, images were captured using a Hitachi S3000N scanning electron microscope at an acceleration of 20 kV at different magnification at Walter Sisulu University, South Africa. Gold sputtering for the SEM analysis was done using a SC7640 Auto/Manual high-resolution super coater (Quorum Technology Ltd., England) at a voltage of 2 kV and plasma current of 25 mA for one minute.

2.7.4. XRD Characterization. XRD analysis was done using PANalytical X'Pert Pro powder diffractometer (Fletcher Laboratories Limited, Nairobi, Kenya) and X-ray diffraction spectrometer (PANalytical X'Pert Pro, Netherlands) using Cu-Kα radiation in a range of 2θ. Scans were done in the range 30–80°C at 2θ, with 0.02° step sizes held for 2 seconds each. The size of the ZNPs was determined using Scherrer's formula as shown below:

$$d = \frac{0.89\lambda}{\beta \cos \theta}, \qquad (1)$$

where 0.89 is Scherrer's constant, λ is the wavelength of the X-rays, θ is the Bragg diffraction angle, and β is the full width at half maximum (FWHM) of the diffraction peak corresponding to the plane.

2.8. Application of Zinc Oxide Nanocomposite in the Removal of Dieldrin

2.8.1. Effect of Concentration. Measured 20 ml each of 5 ppm, 10 ppm, 30 ppm, 40 ppm, 50 ppm, 60 ppm, and 100 ppm solutions of dieldrin at 300 K was poured into seven different 250 ml conical flasks. In each sample, 0.1 g of the nanocomposite sorbent was added, and then it was shaken using an overhead shaker at a speed of 1500 rpm for 120 min. The residual dieldrin concentration was then determined.

2.8.2. Effect of Adsorbent Type. 20 ml of 20 ppm solution of dieldrin at 300 K was poured into three different 250 ml conical flasks. In each sample, 0.1 g of the nanocomposite sorbent, activated carbon, and ZNPs were added, respectively, and they were shaken using an overhead shaker at 1500 rpm for 120 min. The residual concentration of the pesticide was then determined after two hours.

2.8.3. Effect of Contact Time. 20 ml aliquot of 20 ppm solution of dieldrin was poured into two beakers. In each beaker, 0.1 g of adsorbent was added to the solutions into the beaker, and then the adsorption process was performed at 1500 rpm. The residual concentration of dieldrin was determined after 30, 50, 80, 110, 120, 150, and 180 minutes.

2.8.4. Effect of Temperature. 20 ml aliquot of 20 ppm solution of dieldrin was poured into five different beakers, and 0.1 g of nanocomposite was added to the mixture. Adsorption was performed at 293 K, 300 K, 308 K, 318 K, and 323 K within a contact time of 120 min. The residual concentration of dieldrin was then determined.

2.8.5. Effect of Adsorbent Dosage. Measured 20 ml of 20 ppm solution of dieldrin at 300 K was poured into six different 250 ml conical flasks. In each sample, 0.01 g, 0.02 g, 0.04 g, 0.08 g, 0.1 g, and 0.12 g of nanocomposite sorbent were added, respectively, and they were shaken using an overhead shaker at 1500 rpm for 120 min. The residual concentration of the pesticide was then determined after two hours.

2.8.6. Effect of pH. 20 ml of 20 ppm solution of dieldrin was poured into six different beakers. Then, 0.1 g of an adsorbent was added into each beaker with pH of 1, 3, 4, 7, 10, and 14. Adsorption was performed at room temperature within a contact time of 120 minutes. The residual concentration of dieldrin was then determined.

2.9. Gas Chromatography-Mass Spectrometry Analysis for Residual Concentration of Dieldrin after Batch Adsorption. The samples after the batch adsorption process were ultrafiltrated using filters of size 0.22 μm to remove interference that would block the column of the GC. External standard calibration procedure was used for the quantification process. Series of working solutions of each standard were injected, and responses of peaks were plotted against the peak height. The calibration curve was restricted to the linear range. Residual dieldrin concentration was analyzed using a gas chromatograph coupled with a mass spectrometer and a capillary column with 5% phenyl stationary phase and 95% methylpolysiloxane, with helium as a carrier gas at a flow rate of 1.0 mL/min [34], where the injector temperature was maintained at 270°C. Oven temperature programming began at 100°C (1 min), with a heating rate of 20°C/min to 200°C (2 min) followed by a heating rate of 10°C/min to 280°C (1 min). The total analysis time was 17 min. Aliquots of 1 μL was injected into the GC-MS.

3. Data Analysis

Instrumental data were analyzed and compared with existing data from literature. XRD spectral data were analyzed using Scherrer's formulae [35] to determine the size of the synthesized crystals. The quantity of the pesticide adsorbed by the adsorbent in milligram per gram of the adsorbent and the percentage removal were calculated using the following equations:

$$q_e = \frac{(C_o - C_e)V_m}{m}, \qquad (2)$$

where C_e (mg L^{-1}) is the liquid-phase concentration of dieldrin at any time and C_o (mg L^{-1}) is the initial concentration of the dieldrin in solution. V is the volume of the solution (L), and W is the mass of dry adsorbent (g).

$$\%R = \frac{(C_o - C_e)}{C_o} \times 100, \qquad (3)$$

where C_o and C_e (mg L^{-1}) are the liquid-phase concentrations of dieldrin initially and at equilibrium, respectively.

4. Results and Discussion

4.1. Classical Phytochemical Analysis of C. quadrangularis Leaf Extract. Qualitative screening of C. quadrangularis as in Table 1 showed that the methanolic leaf extract contained proteins, flavonoids, alkaloids, carbohydrates, phenols, tannins, and terpenes, whereas the ethanolic leaf extract of C. quadrangularis contained all the phytochemicals in the methanolic extract except saponins. Cardiac glycosides were not present in both the methanolic and ethanolic extracts. These results agree with previous studies on C. quadrangularis, which showed that the methanolic and ethanolic extracts of this plant contain saponins, alkaloids, tannin, steroids, and flavonoids. These results confirmed that the plant extract contained secondary metabolites and was thus suitable for use as a capping and stabilizing agent in the synthesis of nanoparticles [29].

TABLE 1: Secondary metabolites in methanolic and ethanolic extracts of *C. quadrangularis* leaves.

Phytochemical	Methanolic extract	Ethanolic extract
Cardiac glycosides	−	−
Proteins	++	+
Flavonoids	+	+++
Alkaloids	+	+++
Saponins	++	−
Phenols	+	+++
Tannins	+	+
Carbohydrates	+	−
Terpenes	++	+

Key: +++ = abundant; ++ = moderate; + = least; − = not detected.

4.2. Characterization of the ZNPs, Activated Carbon, and Nanocomposite

4.2.1. UV-Vis Spectrometry.

In the green synthesis of ZnO NPs, *C. quadrangularis* plant extract was employed. The color of the reaction mixture changed from pale yellow to dark brown after adding zinc nitrate powder to the plant leaf extract, suggesting the synthesis of ZnO NPs [17]. The presence of various phytochemicals with different functional groups enhances the reduction of the bulk metal form to nanoscale [36]. Figure 1 shows the UV-Vis spectrum of ZNPs. The spectrum revealed a characteristic absorption peak at 338 nm, which can be assigned to the intrinsic band-gap absorption of ZnO due to the electron transition from the valence band to the conduction band as reported by Khorsand Zak et al. [37]. A similar result was observed by Yedurkar et al. [16] after synthesizing ZNPs using the leaf extract of *Ixora coccinea*. The excitation wavelength at 290 nm (Figure 1) can be attributed to the ZNP suspension in methanol. This has been illustrated by Chen et al. [38] who observed the absorption peak of ZNPs at the excitation wavelength of 285 ± 5 nm. This confirms the UV radiation absorption properties of ZNPs and also explains their use as UV radiation protection agents in sunscreen products [39]

4.2.2. Particle Size Analysis of the Adsorbents.

Figures 2–4 show the particle size analysis of the ZNPs, activated carbon, and nanocomposite. The synthesized nanoparticles as shown in Figure 2 had a mean radius of 14.84 nm, indicating that *C. quadrangularis* had the phytochemicals needed for conversion to ZNPs, whereas the synthesized activated carbon from maize cobs had a mean radius of 9 μm as shown in Figure 3. The particle size distribution of the nanocomposite as shown in Figure 4 was not uniform, given the difference in size of the activated carbon (micro range, Figure 3) and the ZNPs (nano range, Figure 2). Comparatively, the ZNPs had uniform distribution within the nanoscale, whereas the activated carbon from maize cobs had a nonuniform distribution of its porous constituents. This nonuniform distribution of the particles of activated carbon caused the size distribution of the synthesized ZNPs to have a nonuniform distribution of the particles.
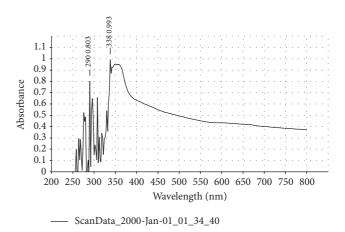

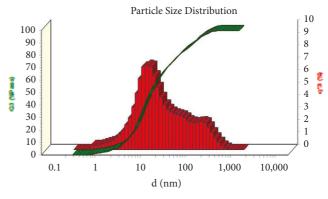FIGURE 1: UV-Vis spectrum of ZNPs.

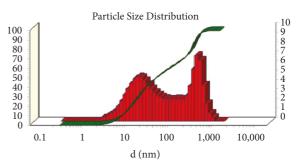FIGURE 2: Particle size analysis of ZNPs.

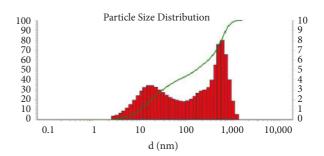FIGURE 3: Particle size analysis of activated carbon.

FIGURE 4: Particle size analysis of zinc oxide-activated carbon nanocomposite.

4.2.3. Fourier Transform Infrared Spectroscopy.

4.2.3. Fourier Transform Infrared Spectroscopy. Figure 5 shows the FTIR spectrum of the synthesized ZNPs. The FTIR bands were at 3401 cm^{-1}, which corresponded to O-H stretch; 2935 cm^{-1} corresponding to bending vibrations (C-H); 1666 cm^{-1} C=O stretch; and 1641 cm^{-1} C=C stretch. Characteristic vibrations at 459 cm^{-1} and 1075 cm^{-1} correlated with Zn-O stretching vibration. Therefore, the vibration bands (Figure 5) indicate the presence of alcohol, alkyl, carboxylic acids, amides, ketones, aldehydes, esters, and aromatic rings, which are believed to be originated from the plant extract that was used during the synthesis of zinc oxide [39].

The FTIR spectrum of the activated carbon synthesized from maize cobs is shown in Figure 6. The mesoporous activated carbon shows a stretch vibration absorption spectrum of O-H at 3740 cm^{-1}. The peak at 1837 cm^{-1} belongs to the nonsymmetric vibration of the C=O group, and the peak at 1740 cm^{-1} represents the stretching vibration absorption of the C=O group. The strong absorption peak at 1620 cm^{-1} for the activated carbon from maize cobs is the result of the presence of vibration stretch of the benzene ring skeleton. Besides, there is also a C-H symmetric stretch vibration peak at 2800 cm^{-1}.

The FTIR spectrum of the formulated ZnO nanocomposite is presented in Figure 7. The broad spectrum at 3429 cm^{-1} corresponds to hydroxyl group vibration stretch [11]. The peaks at 2965 cm^{-1} and 2898 cm^{-1} are attributed to the stretch vibration of C-H group; and the peaks at 1597 cm^{-1} and 1409 cm^{-1} are attributed to the asymmetric and symmetric vibration stretch of O-C-O group, respectively [11]. The peaks that were observed at 1090 cm^{-1} and 892 cm^{-1} are the result of C-O bonds and epoxy groups, respectively, whereas the absorption bands observed at 400–600 cm^{-1} are assigned to the stretching vibration of Zn-O [40]. These results provide evidence that activated carbon was indeed coated to the ZNPs, and this agreed with the XRD and SEM results.

In the ZnO nanocomposite, a shift of hydroxyl group vibration to a higher wavenumber is observed (from 3401 cm^{-1} to 3429 cm^{-1}). This shift is due to an increment in the positive charge of the hydroxyl group adsorbed onto the surface of the composite, confirming the acid-base property of the adsorbent. The increase in the positive charge of the hydroxyl group on the composite would enhance its affinity for positively charged compounds that will then increase their adsorptivity on the adsorbent [41].

4.2.4. SEM Analysis.

4.2.4. SEM Analysis. The morphology and microstructural analysis of the formulated ZNPs were analyzed using scanning electron microscopy, and the images are shown in Figures 8(a) and 8(b). The images in Figure 8 showed formation of dense nanoclusters comprising of closely packed ZNPs in a more closely similar manner to nanorods having different diameters as shown in Table 2. These nanoparticles aggregated to form secondary particles, which was caused by their high surface energy and small size.

The SEM images depicted that the ZNPs and activated carbon are mixed together to form a composite of different
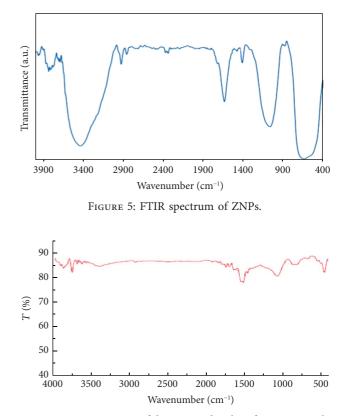

FIGURE 5: FTIR spectrum of ZNPs.

FIGURE 6: FTIR spectrum of the activated carbon from maize cobs.
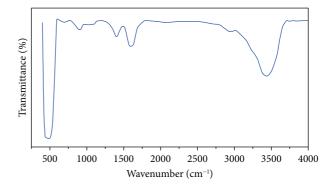

FIGURE 7: FTIR spectrum of the zinc oxide nanocomposite.

sizes and morphologies, which arises from different materials used in the synthesis [19]. The agglomerated particles are close with one another to form a foam-shaped structure with voids. The presence of these voids in the nanocomposite is attributed to migration of vacancies from the activated charcoal pores or nanoparticle grain boundary [42]. From Figures 8(c)–8(f), there was no change in surface topography of the activated carbon after the chemical treatment [43]. The surface of the activated carbon is known to be rough with a heterogenous nature. The rough surface can be occupied by ZNPs. Moreover, the carboxylic functional groups of the activated carbon are responsible for the physical interactions with the nanoparticles, hence causing stabilization of the nanocomposite [43]. Since the nanocomposite
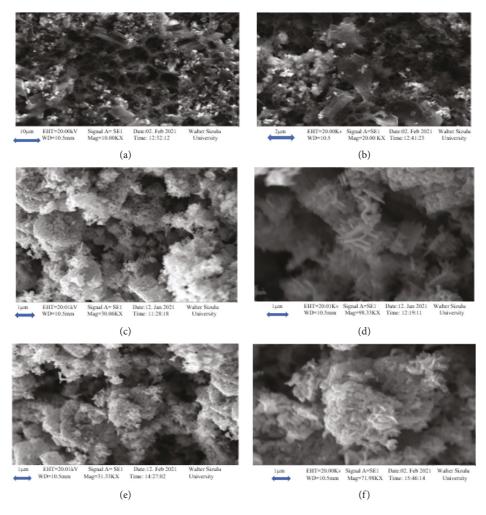
FIGURE 8: Scanning electron microscopy image of ZnO nanoparticles at different resolutions (a, b), as well as at different magnifications (c-f).

TABLE 2: Standard data of hexagonal ZnO from JCPDS (A) and recorded data of the synthesized ZnO nanoparticles from this experiment (B).

A				B			
Hexagonal wurtzite ZnO (JCPDS no. 00-036-1451)				Recorded data of ZNPs			
d(.)	$2(\theta)$	Hkl	Intensity	d(.)	$2(\theta)$	Hkl	Intensity
2.8140	31.770	100	57	2.9512	30.29	100	57.3
2.60332	34.422	002	44	2.5959	34.55	002	47.4
2.47592	36.253	101	100	2.4837	36.17	101	5.3
1.9114	47.539	102	23	1.8980	47.93	102	19
1.62472	56.603	110	32	1.6300	56.45	110	29
1.47712	62.864	103	29	1.5019	61.77	103	27
1.40715	66.380	200	4	1.3883	67.47	112	3.2
1.35825	69.100	201	11	1.3447	69.96	201	4.7

has voids and holes in its SEM structures (Figures 8(c)–8(f)), it is expected to have micropore surface areas, which is ideal for commercial adsorbents [33]. This surface structure is very ideal for the development of materials for the remediation of contaminants in the environment because of their large surface area and stability.

Since there is aggregation of these particles, it implies that the actual size of these nanoparticles is very difficult to calculate from SEM analysis, hence necessitating the use of XRD spectrum to calculate the estimated size of these particles [44]

4.2.5. X-Ray Diffraction Spectroscopy. The crystallinity of the synthesized ZNPs was confirmed using XRD, and the results are shown in Figure 9. XRD analysis was also necessitated because aggregation of nanoparticles makes it difficult to calculate their actual size from SEM analysis. A definite broadening of the line of the XRD peaks indicates that the synthesized materials were in the nanoscale [45]. The peaks that were found to be significant were in agreement with those of JCPDS file no. 00-036-1451 [37, 46], as shown in Table 2. From the XRD spectrum pattern analysis, the peak intensity, full width at half maximum (FWHM) data and position, and the diffraction peaks located at 31.19°, 34.55°, 36.17°, 47.93°, 56.45°, 61.77°, 67.47°, and 69.96° have been keenly indexed as the hexagonal wurtzite phase of ZnO with lattice constants $a = b = 0.324$ nm and $c = 0.521$ nm (JPCDS card number: 36–1451) and correspond to peaks of 100, 002,

101, 102, 110, 103, 112, and 200, respectively (Table 2). Small variation of the intensity might have been brought about by agglomeration and aggregation of the synthesized nanoparticles before actual XRD analysis [47]. The mean particle size of the sample was found to be 22.21 nm, which was derived from the FWHM of the most intense peak corresponding to the peak at 31.19° of the referenced standard peak using Scherrer's formula. From the XRD spectrum of the synthesized activated carbon derived from maize cobs, the diffraction peaks at 24.28θ and 44.77θ are indexed to 002 and 100 XRD spectra of pure activated carbon [33]. The XRD pattern showed an amorphous state of the obtained activated carbon from maize cobs. There was no graphitization that occurred during the carbonization or activation process. An increase in the sharpness and intensity of the peak indexed to 100 XRD spectrum of pure activated carbon shows that the activated carbon tends to crystallize though in a non-graphitized structure [33] behavior. The ZnO/AC nanocomposite pattern shows two wide diffraction peaks of 34.15 and 38.00 at 2θ, which are related to (002) and (101) of the pure carbon and hexagonal wurtzite phase of zinc oxide (JPCDS card number: 36–1451), respectively, which indicated the formation of the nanocomposite in the process.

Figure 9(c) shows the XRD patterns of the ZnO/AC composite produced by the green synthesis method. From the spectrum patterns, the sample entirely exhibits the patterns assigned to a well-crystalline hexagonal phase of ZnO. The strong and narrow diffraction peak is an indicator that the material has a good crystallite structure. No characteristic peaks of impurities such as zinc hydroxide were detected. When activated carbon was introduced to the zinc oxide nanoparticles, the size of the nanoparticles decreased from 22.21 nm to 16.32 nm. This potentially solves the problem of zinc oxide nanoparticle aggregation because the large specific surface area and high surface energy of activated carbon weaken this tendency [20], thereby increasing the reaction surface area.

4.2.6. FTIR Adsorption Analysis of Dieldrin.

From the FTIR analysis of the nanocomposite, it was noted that indeed the adsorption of dieldrin occurred on the surface of the adsorbent. This is indicated by the presence of a peak at 669 cm^{-1}, which is attributed to stretching of alkyl halide bonds, of which one of the bonds is in the dieldrin structure [48]. The nanocomposite after adsorbing dieldrin showed spectroscopic peaks at the following wavenumbers on the FTIR spectrum: 422, 669, 1017, 1375, 1458, 2917, 2949 cm^{-1} for Zn-O stretch, C-H bend alkenes, C-Cl stretch alkyl halides, =C-H bend alkenes, C-H rock, C-C stretch vibrations, C-H rock alkanes, C-H bend alkanes, CH_2 stretch alkanes, and CH_3 stretch of alkanes, respectively, as shown in Figure 10 [48].

Before adsorption using activated carbon, there was absence of a peak at a wavenumber of 600 cm^{-1} that is attributed to the presence of alkyl halides stretch arising from dieldrin contact with the adsorbent. This was observed in the spectrum of the activated carbon after adsorption of dieldrin (Figure 11). Activated carbon after adsorbing dieldrin showed the following spectroscopic peaks at the following

wavenumbers on the FTIR spectrum: 600, 981, 1057, 1670, and 3198 cm^{-1} for C-Cl stretch alkyl halides, =C-C bend of alkenes, =C-H bend alkenes, C-H rock, C-H stretch, C-C stretching, -C=C stretch, and -OH stretch, respectively [48].

Nanoparticles after adsorbing dieldrin showed spectroscopic peaks at the following wavenumbers on the FTIR spectrum: 484, 669, 1077, and 1668 cm^{-1} for Zn-O stretch, C-Cl stretch alkyl halides, =C-H bend alkenes, C-H rock, C-O stretch, and O-H stretch, alcohols and phenols, respectively, as shown in Figure 12 [49]. From Figure 5, the FTIR spectrum before adsorption of dieldrin using ZNPs, there was absence of C-Cl stretch for alkyl halides that has appeared at a wavenumber of 669 cm^{-1} after adsorption of dieldrin.

4.2.7. GC-MS Data.

The GC-MS analysis using a capillary column with 5% phenyl stationary phase and 95% methylpolysiloxane, with helium as a carrier gas, indicated the presence of dieldrin (main peak, $t_R = 15.496$ min, m/z 378, peak area 41783) using single ion monitoring for the standards [50]. The residual concentration was also determined under the same conditions and technique. The GC-MS spectrum sample for the dieldrin sample of 200 ppm is presented in Figure 13, and the GC-MS spectrum of the 200 ppm of the dieldrin after adsorption is presented in Figure 14.

4.3. Adsorption Studies

4.3.1. Effect of pH.

The pH of the aqueous solution is expected to affect the removal of the pesticide by the adsorbent from the solution due to its influence on both the surface-binding sites of the adsorbent and the ionization process of dieldrin molecules [51]. The effect of pH on the adsorption of dieldrin at equilibrium (q_e) and efficiency removal by nanocomposite is shown in Figure 15.

At pH values less than 3, calculated q_e values are also found to be low. This is due to the cationic pesticide reaction with hydroxyl ions [52]. In acidic conditions, hydrogen ions are produced in the solution [15]. The positive charges are aggregated on the surface of the adsorbent surface, hence lowering adsorptivity of pesticide ions onto the surface of the adsorbent arising from electrostatic repulsion and the competition between H^+ ions and dieldrin ions for the adsorption sites [51]. On the other hand, when the pH of the solution is increased, the surface of the adsorbent becomes more negatively charged because of subsequent attraction of dieldrin ions to the positive charge, thus favoring the adsorption process [15]. Optimum adsorption capacity was observed at a pH of 7. A decrease in the adsorption capacity at high pH may be attributed to the inhibition of the adsorption because of the soluble hydroxyl complexes from the hydroxyl functional groups of sodium hydroxide that was used in raising the pH [51]. The optimum adsorption capacity of nanocomposite was found to be 4.0 mg/g at pH 7. The percentage adsorption of dieldrin pesticide onto nanocomposite was found to be 73.98, 91.16, 95.21, 99.95, 99.47, and 86.53% for solutions of pH 1, 3, 4, 7, 9, and 14,
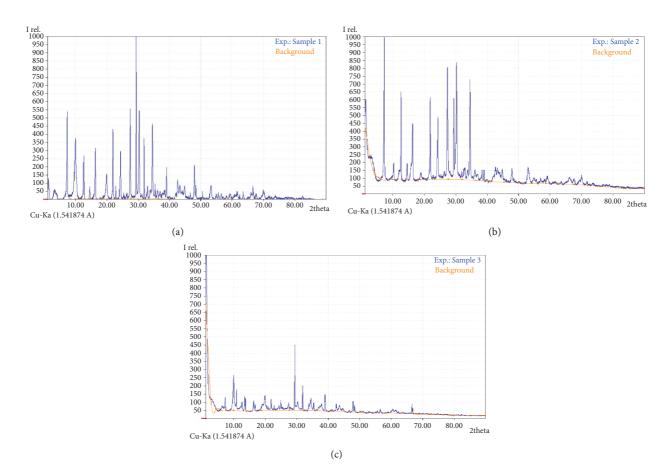
(a)

(b)

(c)

FIGURE 9: XRD spectrum of (a) ZNPs, (b) activated carbon, and (c) zinc oxide-activated carbon nanocomposite.
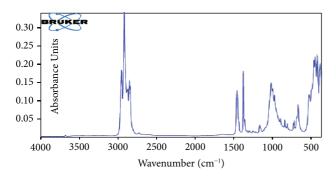

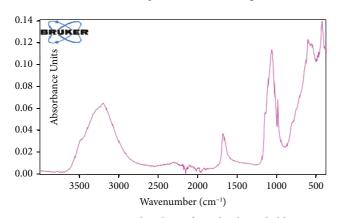FIGURE 10: Nanocomposite after adsorbing dieldrin.
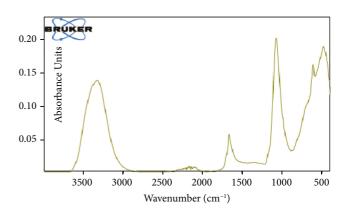

FIGURE 12: Nanoparticle after adsorbing dieldrin.

FIGURE 11: Activated carbon after adsorbing dieldrin.

respectively. Thus, all the adsorption experiments were performed at pH 7. In other experiments for other reaction parameters, the pH of original dieldrin solution was 7.0 and it was not changed.

4.3.2. Effect of Pesticide Concentration and Contact Time.

A graph of amount adsorbed against contact time at different initial dieldrin concentrations is presented in Figure 16. It is observed that optimum adsorption was achieved after a contact time of 120 min and that the adsorption process proceeded in three cycles. An initial slow phase (30–80 min), a subsequent fast phase (80–110 min), and a final plateau
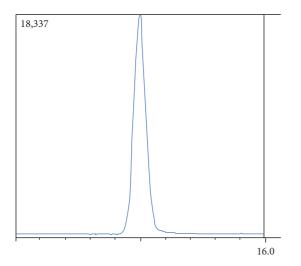
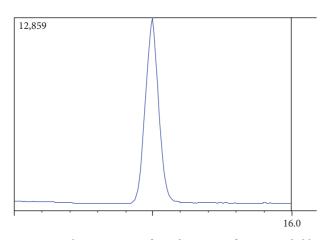FIGURE 13: GC-MS chromatogram of dieldrin standard of 200 ppm.

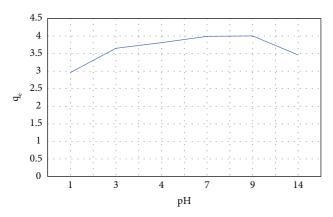FIGURE 14: Chromatogram after adsorption of 200 ppm dieldrin standard using ZnO nanocomposite.

FIGURE 15: Effect of pH on adsorption of dieldrin onto nanocomposite.

phase (>120 min) were observed when the adsorption is in a state of equilibrium where dieldrin desorption and adsorption are equal. In the first cycle adsorption, the molecules of dieldrin rapidly move to the adsorbent surface by mass transfer because of the vacant adsorption sites on the adsorbent [15]. Thereafter, there is a slow diffusion from the boundary layer in the second cycle to the surface of the adsorbent since majority of the surface are covered and finally diffuse into the porous structure of the adsorbent [15].

Figure 17 shows the adsorption levels against initial dieldrin concentrations at 27°C. The amount of dieldrin adsorbed (mg/g) increased with an increase in initial dieldrin concentrations at subsequent fast phase (80–110 min). The amount of dieldrin removed increased from 1.0 mg/g to 19.8 mg/g with an increase in dieldrin concentration in the range 5–100 mg/L. It is observed that the adsorption of dieldrin depends on the initial concentration of the pesticide. When the concentration of the dieldrin solution is increased, the rate of adsorption increases because of enhanced mass transfer driving the molecules to the adsorbent's adsorbing sites [6]. However, it is observed that the percentage removal of pesticides decreased with an increase in pesticide concentration. When the initial dieldrin concentration was increased from 5 to 100 mg/L, the percentage removal decreased from 99.93 to 99.00%. This resulted from the saturation of the adsorption sites when the concentration of dieldrin increased. However, higher dieldrin adsorption yields were recorded at lower dieldrin concentrations.

4.3.3. Effect of Temperature. Temperature as one of the physicochemical parameters affecting the adsorption of dieldrin onto the formulated nanocomposite was studied at 20, 37, 35, 45, and 50°C. The findings are shown in Figure 18. The experimental findings show that the extent of adsorption is directly proportional to the temperature of the system during adsorption. The temperature influenced adsorption in two ways. Increasing the temperature increases the rate of motion of the dieldrin molecules through the boundary layer and in the sorption sites of the adsorbent, owing to the decrease in the viscosity of the solution for highly concentrated solutions [21]. Further to this, optimizing the temperature will also eventually cause a shift in the equilibrium capacity of the adsorbent [21]. The adsorption of dieldrin onto the nanocomposite is increased from 3.63 mg/g (90.79% removal) to 3.79 mg/g (94.91% removal) when the temperature was increased from 20 to 50°C at an initial concentration of 20 mg/L. The highest adsorption capacity was found at a temperature of 27°C with 3.91 mg/g (97.72% removal) adsorption capacity; hence, all other batch reactions were performed at this temperature as the optimized temperature.

4.3.4. Effect of Amount of Adsorbent. The influence of adsorbent dosage on the efficiency of dieldrin removal is shown in Figure 19. The adsorbent dosage was varied from 0.01 to 0.12 g. The results are presented in Figure 19, which shows that the adsorption yield of dieldrin is directly proportional to the amount of adsorbent used in the adsorption process. When the adsorbent concentration was increased from 0.01 to 0.1 g/L, the removal increased from 94.99 to 99.98%. This may arise from the fact that the higher the doses of the adsorbent, the more the sorbent surfaces that will be available for adsorption.
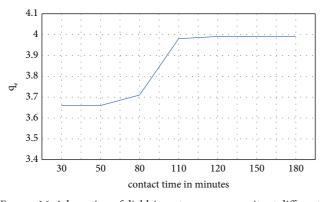
FIGURE 16: Adsorption of dieldrin onto nanocomposite at different contact times.
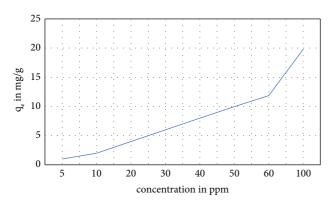

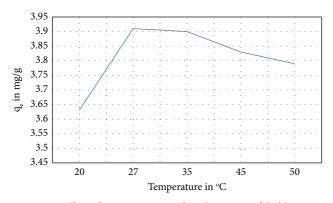FIGURE 17: Effect of concentration on adsorption of dieldrin.

FIGURE 18: Effect of temperature on the adsorption of dieldrin onto nanocomposite (adsorbent dosage = 0.1 g/20 mL, pH = 7.0, contact time = 120 min).

4.3.5. Type of Adsorbent.

The three adsorbents synthesized were used in the adsorption of dieldrin at the optimized parameters. Figure 20 shows activated carbon improved the adsorption capacity of the nanoparticle. Preparing a composite of activated carbon and nanoparticle changed the adsorption capacity from 3.72 mg/g (93.11% removal) to 4.0 mg/g (99.97% removal). The percentage removal increased because activated carbon is a very good adsorbent material due to its porous structure [53], hence more adsorbing sites compared with zinc oxide nanoparticles.
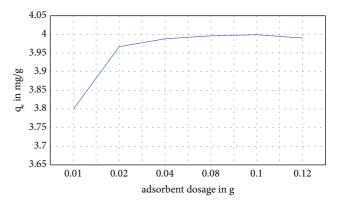

FIGURE 19: Effect of adsorbent dosage on the adsorption of dieldrin onto nanocomposite (initial concentration 20 ppm, pH = 7.0, contact time = 120 min).

4.4. Kinetics Models.

Three kinetic models were modelled to examine the controlling mechanisms of adsorption process based on the experimental data. The pseudo-first-order and pseudo-second-order equations were used to analyze the adsorption kinetics of the process. The pseudo-first-order kinetic model is shown in equation (4) [15]:

$$\ln(q_e - q_t) = \ln q_e - k_1 t, \tag{4}$$

where q_e and q_t are the amounts of pesticide adsorbed (mg/g) at equilibrium and at time t (h), respectively, and k_1 is the rate constant of adsorption (h^{-1}). Values of k_1 were calculated from the plots of $\ln(q_e - q_t)$ against t for various initial concentrations at 27°C.

The pseudo-second-order kinetic model is shown in equation (5) [54]:

$$\frac{t}{q_t} = \frac{1}{k_2 q_e^2} + \frac{1}{q_e} t, \tag{5}$$

where k_2 is the pseudo-second-order constant (g/(mg h)) and is calculated from the slope and intercept of plot t/q_t versus t. [6]

The intraparticle rate is calculated using equation (6) [55], which was designed by Webber and Morris:

$$q_t = k_{int} t^{1/2} + c, \tag{6}$$

where k_{int} is the rate constant of intraparticle diffusion (mg/(gh$^{1/2}$)), which is determined from the slope of a plot of q_t against $t_{1/2}$ [55]

The suitability of fitting of these models to the experimental findings was assessed by fitting the data to the linearized forms of the kinetic models, i.e., plot of $\ln(q_e - q_t)$ against t, (t/q_t) versus t, and q_t against $t^{1/2}$, respectively, as well as the regression coefficients for each expression.

From adsorption kinetics results, we can find that the amount of mass transfer of adsorbate per time that is helpful in determining the adsorption rate [56]. In this work, linearized pseudo-first-order, pseudo-second-order, and intraparticle diffusion models were tested to check their applicability (Figures 21–23). The pseudo-first-order
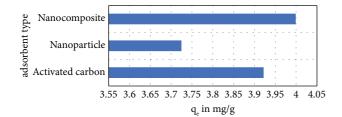
FIGURE 20: Effect of adsorbent type on the adsorption of dieldrin onto nanocomposite (adsorbent dosage = 0.1 g/20 mL, pH = 7.0, contact time = 120 min, temperature 27°C).

kinetic model assumed that adsorption of dieldrin onto a nanocomposite is directly proportional to the number of sorption sites on the sorbent [24]; in contrast, the pseudo-second-order kinetic model assumed that chemical adsorption takes place when valence electrons of the adsorbent and the adsorbate are shared during the adsorption process. The best-fit model is adopted depending on the linear correlation coefficient R^2 values. Adsorption kinetics is important as it helps rating the efficiency of the sorption process [57]. The results presented in Table 3 showed that the pseudo-second-order model was more applicable for the adsorption of dieldrin. The correlation coefficient R^2 values of the pseudo-second-order model from experimental data were closer to a whole number 1, which is better than those of the pseudo-first-order model. The q_e determined from the pseudo-second-order kinetic model was much closer to that q_e determined experimentally, which is better than that from the pseudo-first-order model. The pseudo-first-order and pseudo-second-order models are applicable to physisorption and chemisorption processes, respectively [10]. Hence, it can be reported that this adsorption process of dieldrin ions onto a nanocomposite is a chemisorption process, which involved sharing of electrons of the adsorbent and adsorbate in the reaction system [58].

4.5. Thermodynamic Analysis.

To determine whether the adsorption process will occur spontaneously, a set of thermodynamic parameters for the dieldrin adsorption system by nanocomposite was calculated, including changes in the standard Gibbs free energy ($\Delta G°$), enthalpy ($\Delta H°$), and entropy ($\Delta S°$). The Gibbs free energy is calculated using the following equation:

$$\Delta G° = -RT \ln K_c, \tag{7}$$

where R is the universal gas constant (8.314 J/(mol/K)) and T is the temperature (K). The values of $\Delta H°$ and $\Delta S°$ were calculated from the intercept and slope of a plot of $\Delta G°$ versus T by linear regression analysis of the equation below:

$$\Delta G° = \Delta H° - T\Delta S°. \tag{8}$$

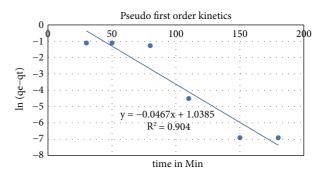The constant of equilibrium (K) of the adsorption is calculated as follows:

FIGURE 21: Pseudo-first-order kinetic fit for adsorption of 20 ppm of dieldrin solution onto nanocomposite at 27°C.
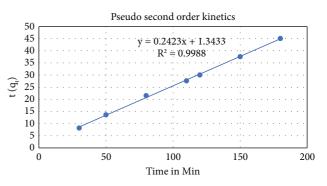

FIGURE 22: Pseudo-second-order kinetic fit for adsorption of 20 ppm of dieldrin solution onto nanocomposite at 27°C.

FIGURE 23: Intraparticle diffusion model for adsorption of 20 ppm of dieldrin solution onto nanocomposite at 27°C.

$$K_c = \frac{C_i}{C_r}, \tag{9}$$

where C_i and C_r are the dieldrin concentration on the adsorbent and residual dieldrin concentration at equilibrium, respectively [51]. In this case, the activity was used instead of concentration in order to obtain the standard thermodynamic equilibrium constant (K_c) of the adsorption system [51].

The data obtained from adsorption isotherm models were conveniently used to determine parameters of thermodynamics such as standard Gibbs free energy ($\Delta G°$), enthalpy ($\Delta H°$), and entropy ($\Delta S°$). The Gibbs free energy

TABLE 3: Kinetic parameters for adsorption of dieldrin onto nanocomposite.

Conc. (ppm)	Pseudo-first-order			Pseudo-second-order					Intraparticle diffusion		
	K_{ad}	q_e	R^2	K	q_e	h	$q_e\ exp$	R^2	K_p	C	R^2
20	0.072	0.8980	0.9040	0.2423	2.35 mg/g	1.3433	4 mg/g	0.9988	15.275	49.078	0.8194

TABLE 4: Thermodynamic data of the batch adsorption experiment of dieldrin onto nanocomposite.

Concentration ppm	$\Delta G°$ (kJ/kmol)			Thermodynamics measurements	
	300 K	308 K	318 K	$\Delta H°$ (kJ/mol)	$\Delta S°$ (J/mol K)
10	−5.742	−5.894	−6.072	−0.25	0.01
20	−7.415	−7.607	−7.808	−0.89	0.02
30	−8.48	−8.706	−8.978	−0.19	0.03
60	−10.181	−10.451	−10.742	−0.86	0.03

shows the degree of ease of adsorption process. [54]. As shown in Table 4, the calculated negative value of Gibbs free energy for dieldrin adsorption onto the nanocomposite showed the possibility of the adsorption process and spontaneous nature of the adsorption [18]. The possibility of the adsorption process increased with increasing temperature [21]. When the temperature is increased, the kinetic energy of molecules is increased, hence increasing the rate of reaction. The negative value of $\Delta H°$ indicated that this adsorption process was exothermic [59]. This was confirmed with increased adsorption capacity from 3.63 to 3.91 mg/g when the temperature was increased from 293 to 400 K. The positive value of $\Delta S°$ indicated an increase in randomness at the solid/solution interface during the adsorption process [60]. This occurred due to the redistribution of energy between the adsorbate and the adsorbent [54]. Thus, adsorption is likely to occur spontaneously at normal and high temperatures because $\Delta S° > 0$ [18]

4.6. Isotherm Modelling

4.6.1. Langmuir Isotherm Analysis.
Langmuir derived a model for monolayer adsorption of particles onto an adsorbent with a homogenous surface with a fixed number of adsorption sites without lateral interaction [18]. This model postulated that all the adsorbing sites have equal energies. This model also postulated that the interaction among molecules reduces with increased distance. The linearized Langmuir model is represented as follows:

$$\frac{c_e}{q_e} = \frac{1}{k_l b} + \frac{c_e}{b}, \tag{10}$$

where C_e is the concentration of the adsorbate at equilibrium (mg/l), q_e is the amount of adsorbate adsorbed at equilibrium (mg/g), b is the capacity of the monolayer of the adsorbent (mg/g), and K_l is the Langmuir adsorption equilibrium constant (l/mg) measuring intensity of the adsorption process. A plot of C_e/q_e versus C_e yields the values of b and K_l from the gradient and intercept, respectively [9].

The Langmuir isotherm essential characteristics has been expressed in terms of equilibrium parameter separation factor (R_L), which is defined by the following equation to check the feasibility of the reaction:

$$R_L = \frac{1}{1 + K_l C_O}, \tag{11}$$

where K_l is the Langmuir constant and C_o is the highest pesticide concentration (mg/l). The value of R_L indicates the type of the isotherm to be either favorable ($0 < R_L < 1$), or unfavorable ($R_L > 1$), or linear ($R_L = 1$), or irreversible ($R_L = 0$).

4.6.2. Freundlich Isotherm Analysis.
This model assumes a multilayer adsorption process onto a heterogenous adsorbent with a nonuniform distribution of adsorption energies [52]. This model postulated adsorption of the energetically favored binging sites first as the binding strength reduces sequentially with increased coverage of these sites [61]. The linearized Freundlich model is represented as follows:

$$\log q_e = \log k_f + \frac{1}{n} \log c_e, \tag{12}$$

where k_f (mg/(g(mg/l)$^{1/n}$)) and n are the constants of Freundlich adsorption isotherm, indicating the capacity of adsorption and adsorption intensity. k_f gives a measure of bonding energy, which is a measure of distribution coefficient during adsorption that helps in determining the quantity of dieldrin adsorbed at equilibrium [61]. The gradient $1/n$ is an irrational fraction that varies between 0 and 1, which measures the adsorption capacity and the nature of adsorption surface. A value of $1/n$ below one indicates that the adsorption model is applicable to Langmuir isotherm, whereas $1/n$ above 1 indicates Freundlich isotherm. When $\log q_e$ was plotted against $\log C_e$, a straight line with slope of $1/n$ and intercept of $\log k_f$ was obtained [52].

The Langmuir and Freundlich isotherms for the adsorption of dieldrin at various temperatures were determined through graphical analysis. The R^2 values were determined by fitting the experimental data for the dieldrin adsorption using both the Langmuir and Freundlich isotherms and are presented in Table 5. These findings clearly

TABLE 5: Linear Langmuir and Freundlich isotherm parameters at different temperatures.

Temperature (°C)	Linear Langmuir isotherm			Linear Freundlich isotherm			
	R^2	q_m	b	R^2	k_f	n	R_L for 20 ppm
27	0.8929	2.461	48.54	0.7604	3.525	0.4129	0.043
35	0.8056	2.43	50.74	0.7840	4.496	0.3968	0.038
45	0.7753	2.672	178.21	0.7532	8.346	1.09	0.007

TABLE 6: Comparison of adsorption capacities and other parameters for the removal of dieldrin in different adsorbent materials.

Adsorbent	Adsorbate	Surface area	Adsorption capacity (mg/g)	Concentration range (mg/l)	Contact time (hr)	Temp (°C)	pH	% Adsorption	Reference
Triolein-embedded activated carbon composite	Dieldrin	721	0.002	0.001–0.05	48	25	4–8	—	[6]
Al$_{30}$/bentonite	Dieldrin	164.2	0.188 0.196 0.191	0.2	5	45	7.5	95	[52]
Magnetic nanospheres coated with polystyrene	Dieldrin	129	0.01	1	25			93.3	[62]
Montmorillonite kaolinite clays	Dieldrin/ endrin	14.1		500–5000			5.4–7.2		[6]
Zinc oxide nanoparticles impregnated with pea peels	Chlorpyrifos		47.846				2	56%	[18]
Zinc oxide-activated carbon nanocomposite	Dieldrin		2.35	5–100	3	27	7	97	This work

showed that the adsorption of dieldrin pesticide onto nanocomposite fitted well with the Langmuir model. The fact that the Langmuir model was a good fit to the experimental adsorption data suggested physical adsorption and a homogenous distribution of sorption sites on the nanocomposite [62]. The calculated values of $1/n$ and R_L parameters were in the range of 0 and 1, showing a favorable adsorption of dieldrin onto the nanocomposite [62].

The adsorption capacity of different adsorbents was compared as presented in Table 6.

5. Conclusion

In this work, nanotization of ZnO (using leaf extracts of *Cissus quadrangularis*) combined with activated carbon (derived from *Zea mays* cobs) led to a ZNP-activated carbon nanocomposite with improved capabilities for immobilization of dieldrin both in effectiveness and efficiency. The results confirmed that in the medium treated with activated carbon, ZNPs, and ZNP-activated carbon nanocomposite, dieldrin were remediated *in situ*. The zinc oxide nanocomposite gave the highest remediation activity. The pseudo-second-order model is more appropriate for the adsorption of dieldrin with an R^2 value of 0.9988 and q_e of 2.35 mg/g compared with the pseudo-first-order model with an R^2 value of 0.904 and q_e of 0.898 mg/g. Lastly, the Langmuir model yields a better fit than the Freundlich model as reflected by the correlation coefficient R^2 of 0.8929,

0.8056, and 0.7753 at 27, 35, and 45°C and 0.7604, 0.7840, and 0.7532 at 27, 35, and 45°C for the nanocomposite, respectively. In conclusion, the nanocomposite is better at sorbing dieldrin in solution than activated carbon and nanoparticles. The study recommends testing the remediation potential of the synthesized nanocomposite on other persistent organic pollutants.

Data Availability

The spectroscopic data sets supporting the conclusions of this study are available from the corresponding author upon request.

Conflicts of Interest

The authors declare that they have no conflicts of interest.

Acknowledgments

References

[1] A. Wenaty, A. Fromberg, F. Mabiki, B. Chove, A. Dalsgaard, and R. Mdegela, "Persistent organochlorine compounds levels in selected fish species from Lake Victoria and associated human health risks," *Agriculture, Forestry and Fisheries*, vol. 8, no. 1, pp. 1–9, 2019.

[2] A. Barra Caracciolo, E. Topp, and P. Grenni, "Pharmaceuticals in the environment: biodegradation and effects on natural microbial communities. A review," *Journal of Pharmaceutical and Biomedical Analysis*, vol. 106, pp. 25–36, 2015.

[3] D. Kim, H.-Y. Ryu, J. H. Lee et al., "Organochlorine pesticides and polychlorinated biphenyls in Korean human milk: contamination levels and infant risk assessment," *Journal of Environmental Science and Health, Part B*, vol. 48, no. 4, pp. 243–250, 2013.

[4] S. K. Sagiv, S. W. Thurston, D. C. Bellinger, P. E. Tolbert, L. M. Altshul, and S. A. Korrick, "Prenatal organochlorine exposure and behaviors associated with attention deficit hyperactivity disorder in school-aged children," *American Journal of Epidemiology*, vol. 171, no. 5, pp. 593–601, 2010.

[5] F. R. Boucher and F. G. Lee, "Adsorption of lindane and dieldrin pesticides on unconsolidated aquifer sands," *Environmental Science and Technology*, vol. 6, no. 6, pp. 538–543, 1972.

[6] J. Ru, H. Liu, J. Qu, A. Wang, and R. Dai, "Removal of dieldrin from aqueous solution by a novel triolein-embedded composite adsorbent," *Journal of Hazardous Materials*, vol. 141, no. 1, pp. 61–69, 2007.

[7] S. E. Hearon, M. Wang, and T. D. Phillips, "Strong adsorption of dieldrin by parent and processed montmorillonite Clays," *Environmental Toxicology & Chemistry*, vol. 39, no. 3, pp. 517–525, 2020.

[8] M. Pirbazari and W. J. Weber, "Removal of dieldrin from water by activated carbon," *Journal of Environmental Engineering*, vol. 110, no. 3, pp. 656–669, 1984.

[9] K. Shrivas, A. Ghosale, N. Nirmalkar, A. Srivastava, S. K. Singh, and S. S. Shinde, "Removal of endrin and dieldrin isomeric pesticides through stereoselective adsorption behavior on the graphene oxide-magnetic nanoparticles," *Environmental Science and Pollution Research*, vol. 24, no. 32, pp. 24980–24988, 2017.

[10] R. Ramya, M. Murugan, L. Lajapathirai, and S. Sivasamy, "Activated carbon (prepared from secondary sludge biomass) supported semiconductor zinc oxide nanocomposite photocatalyst for reduction of Cr(VI) under visible light irradiation," *Journal of Environmental Chemical Engineering*, vol. 6, no. 6, pp. 7327–7337, 2018.

[11] H. A. Ismael, E. J. Mohammad, A. J. Atiyah, S. H. Kadhim, and K. J. Kahdum, "Synthesis and characteristic study of composite zinc oxide and functionalized activated carbon with investigation of its adsorption ability: a kinetic study," *IOP Conference Series: Earth and Environmental Science*, vol. 722, no. 1, Article ID 012007, 2021.

[12] C. H. Kim and B.-H. Kim, "Zinc oxide/activated carbon nanofiber composites for high-performance supercapacitor electrodes," *Journal of Power Sources*, vol. 274, pp. 512–520, 2015.

[13] M. Selvakumar, D. Krishna Bhat, A. Manish Aggarwal, S. Prahladh Iyer, and G. Sravani, "Nano ZnO-activated carbon composite electrodes for supercapacitors," *Physica B: Condensed Matter*, vol. 405, no. 9, pp. 2286–2289, 2010.

[14] M. Rani and U. Shanker, "Degradation of traditional and new emerging pesticides in water by nanomaterials: recent trends and future recommendations," *International Journal of Environmental Science and Technology*, vol. 15, no. 6, pp. 1347–1380, 2018.

[15] P. Senthil Kumar, S. Ramalingam, C. Senthamarai, M. Niranjanaa, P. Vijayalakshmi, and S. Sivanesan, "Adsorption of dye from aqueous solution by cashew nut shell: studies on equilibrium isotherm, kinetics and thermodynamics of interactions," *Desalination*, vol. 261, no. 1-2, pp. 52–60, 2010.

[16] S. Yedurkar, C. Maurya, and P. Mahanwar, "Biosynthesis of zinc oxide nanoparticles using Ixora coccinea leaf extract-A green approach," *Open Journal of Synthesis Theory and Applications*, vol. 5, no. 1, pp. 1–14, 2016.

[17] A. A. Alyamani, S. Albukhaty, S. Aloufi, F. A. Almalki, H. Al-Karagoly, and G. M. Sulaiman, "Green fabrication of zinc oxide nanoparticles using phlomis leaf extract: characterization and in vitro evaluation of cytotoxicity and antibacterial properties," *Molecules*, vol. 26, no. 20, Article ID 6140, 2021.

[18] A. ul Haq, M. Saeed, M. Usman et al., "Sorption of chlorpyrifos onto zinc oxide nanoparticles impregnated Pea peels (Pisum sativum L): equilibrium, kinetic and thermodynamic studies," *Environmental Technology & Innovation*, vol. 17, Article ID 100516, 2020.

[19] G. J. F. Cruz, M. M. Gómez, J. L. Solis et al., "Composites of ZnO nanoparticles and biomass based activated carbon: adsorption, photocatalytic and antibacterial capacities," *Water Science and Technology*, vol. 2017, no. 2, pp. 492–508, 2018.

[20] J. Chen, X. Wen, X. Shi, and R. Pan, "Synthesis of zinc oxide/activated carbon nano-composites and photodegradation of rhodamine B," *Environmental Engineering Science*, vol. 29, no. 6, pp. 392–398, 2012.

[21] M. Ghaedi, S. Heidarpour, S. Nasiri Kokhdan, R. Sahraie, A. Daneshfar, and B. Brazesh, "Comparison of silver and palladium nanoparticles loaded on activated carbon for efficient removal of Methylene blue: kinetic and isotherm study of removal process," *Powder Technology*, vol. 228, pp. 18–25, 2012.

[22] J. Mo, Q. Yang, N. Zhang, W. Zhang, Y. Zheng, and Z. Zhang, "A review on agro-industrial waste (AIW) derived adsorbents for water and wastewater treatment," *Journal of Environmental Management*, vol. 227, pp. 395–405, 2018.

[23] G. Madhumitha, G. Elango, and S. M. Roopan, "Biotechnological aspects of ZnO nanoparticles: overview on synthesis and its applications," *Applied Microbiology and Biotechnology*, vol. 100, no. 2, pp. 571–581, 2016.

[24] S. E. A. Elhafez, H. A. Hamad, A. A. Zaatout, and G. F. Malash, "Management of agricultural waste for removal of heavy metals from aqueous solution: adsorption behaviors, adsorption mechanisms, environmental protection, and techno-economic analysis," *Environmental Science and Pollution Research*, vol. 24, no. 2, pp. 1397–1415, 2017.

[25] N. Mayedwa, A. T. Khalil, N. Mongwaketsi, N. Matinise, Z. K. Shinwari, and M. Maaza, "The study of structural, physical and electrochemical activity of zno nanoparticles synthesized by green natural extracts of sagretia thea," *Nano Research & Applications*, vol. 3, no. 2, 2017.

[26] O. Of, "Cissus quadrangularis extract and its various in vitro studies," *Green Synthesis of Zinc Oxide Nanoparticles Using*

Fresh Stem of Cissus quadrangularis Extract and its Various in vitro Studies, vol. 29, no. 6, pp. 1323–1327, 2017.

[27] A. D. R. Eswaran and A. Anandan, "Analysis of chemical composition of cissus quandrangularis Linn by GC-MS," *Asian Journal of Pharmaceutical and Clinical Research*, vol. 5, pp. 2011-2012, 2012.

[28] A. Kumar, M. Rana, T. Joshi, S. Bhoj, and A. J. Rana, "For fracture healing," *Potential of Cissus qudrangularis Transdermal Patch for Fracture Healing*, vol. 18, pp. 121–127, 2018.

[29] S. Dhanasekaran, "Phytochemical characteristics of aerial part of *Cissus quadrangularis* (L) and its in-vitro inhibitory activity against leukemic cells and antioxidant properties," *Saudi Journal of Biological Sciences*, vol. 27, no. 5, pp. 1302–1309, 2020.

[30] S. P. Rajendran and K. Sengodan, "Synthesis and characterization of zinc oxide and iron oxide nanoparticles using Sesbania grandiflora leaf extract as reducing agent," *Journal of Nanoscience*, vol. 2017, Article ID 8348507, 7 pages, 2017.

[31] K. Elumalai, S. Velmurugan, S. Ravi, V. Kathiravan, and G. Adaikala Raj, "Bio-approach: plant mediated synthesis of ZnO nanoparticles and their catalytic reduction of methylene blue and antimicrobial activity," *Advanced Powder Technology*, vol. 26, no. 6, pp. 1639–1651, 2015.

[32] M. J. Ahmed, "Preparation of activated carbons from date (Phoenix dactylifera L.) palm stones and application for wastewater treatments: Review," *Process Safety and Environmental Protection*, vol. 102, pp. 168–182, 2016.

[33] M. Song, B. Jin, R. Xiao et al., "The comparison of two activation techniques to prepare activated carbon from corn cob," *Biomass and Bioenergy*, vol. 48, pp. 250–256, 2013.

[34] A. A. Z. Rodrigues, A. A. Neves, M. E. L. R. De Queiroz, A. F. De Oliveira, L. H. F. Prates, and E. H. D. C. Morais, "Optimization and validation of the salting-out assisted liquid-liquid extraction method and analysis by gas chromatography to determine pesticides in water," *Eclética Química Journal*, vol. 43, no. 1SI, p. 11, 2018.

[35] M. Vaseem, A. Umar, and Y. Hahn, "Preparation and characterization of ZnO nanoparticles by solvent free method," *Contemporary Materials Journal*, vol. 145, no. 7, pp. 582–671, 1988.

[36] K. Handore, S. Bhavsar, A. Horne et al., "Novel green route of synthesis of ZnO nanoparticles by using natural biodegradable polymer and its application as a catalyst for oxidation of aldehydes," *Journal of Macromolecular Science, Part A*, vol. 51, no. 12, pp. 941–947, 2014.

[37] A. Khorsand Zak, R. Razali, W. H. B. Abd Majid, and M. Darroudi, "Synthesis and characterization of a narrow size distribution of zinc oxide nanoparticles," *International Journal of Nanomedicine*, vol. 6, no. 1, pp. 1399–1403, 2011.

[38] X. L. Chen, C. S. Xu, Y. X. Liu et al., "Visible luminescence mechanism of ZnO nanoparticles synthesized by sol-gel method," *Journal of Nanoscience and Nanotechnology*, vol. 11, no. 11, pp. 9415–9420, 2011.

[39] K. H. Sudheer Kumar, N. Dhananjaya, and L. S. R. Yadav, "E. tirucalli plant latex mediated green combustion synthesis of ZnO nanoparticles: structure, photoluminescence and photocatalytic activities," *Journal of Science: Advanced Materials and Devices*, vol. 3, no. 3, pp. 303–309, 2018.

[40] G. T. S. T. da Silva, K. T. G. Carvalho, O. F. Lopes et al., "Synthesis of ZnO nanoparticles assisted by N sources and their application in the photodegradation of organic contaminants," *ChemCatChem*, vol. 9, no. 19, pp. 3795–3804, 2017.

[41] S. Chattoraj, N. K. Mondal, B. Sadhukhan, P. Roy, and T. K. Roy, "Optimization of adsorption parameters for removal of carbaryl insecticide using neem bark dust by response surface methodology," *Water Conservation Science and Engineering*, vol. 1, no. 2, pp. 127–141, 2016.

[42] S. P. Lonkar, V. Pillai, and A. Abdala, "Solvent-free synthesis of ZnO-graphene nanocomposite with superior photocatalytic activity," *Applied Surface Science*, vol. 465, pp. 1107–1113, 2019.

[43] S. Alhan, M. Nehra, N. Dilbaghi, N. K. Singhal, K.-H. Kim, and S. Kumar, "Potential use of ZnO@activated carbon nanocomposites for the adsorptive removal of Cd2+ ions in aqueous solutions," *Environmental Research*, vol. 173, pp. 411–418, 2019.

[44] K. C. Bhainsa and S. F. D'Souza, "Extracellular biosynthesis of silver nanoparticles using the fungus Aspergillus fumigatus," *Colloids and Surfaces B: Biointerfaces*, vol. 47, no. 2, pp. 160–164, 2006.

[45] A. Vishwakarma, "Synthesis of zinc oxide nanoparticle by sol-gel method and study its characterization," *International Journal for Research in Applied Science and Engineering Technology*, vol. 8, no. 4, pp. 1625–1627, 2020.

[46] K. S. Khashan, B. A. Badr, G. M. Sulaiman, M. S. Jabir, and S. A. Hussain, "Antibacterial activity of Zinc Oxide nanostructured materials synthesis by laser ablation method," *Journal of Physics: Conference Series*, vol. 1795, no. 1, Article ID 012040, 2021.

[47] N. Eltugral, H. Simsir, and S. Karagoz, "Preparation of nanosilver-supported activated carbon using different ligands," *Research on Chemical Intermediates*, vol. 42, no. 3, pp. 1663–1676, 2015.

[48] "Table of characteristic IR absorptions,"vol. 3610, Article ID 3640.

[49] H. Agarwal, S. Venkat Kumar, and S. Rajeshkumar, "A review on green synthesis of zinc oxide nanoparticles-an eco-friendly approach," *Resource-Efficient Technologies*, vol. 3, no. 4, pp. 406–413, 2017.

[50] J. M. Rodrigues, E. C. P. Rego, E. F. Guimarães, V. B. Marcus, T. Inmetro, and C. M. Division, "Determination of aldrin purity using a combination of the mass balance approach," *Quantitative NMR*, vol. 26, no. 5, pp. 869–879, 2015.

[51] N. Ertugay and E. Malkoc, "Adsorption isotherm, kinetic, and thermodynamic studies for methylene blue from aqueous solution by needles of pinus sylvestris L," vol. 23, no. 6, pp. 1995–2006, 2014.

[52] R. A. Farghali, M. Sobhi, S. E. Gaber, H. Ibrahim, and E. A. Elshehy, "Adsorption of organochlorine pesticides on modified porous Al30/bentonite: kinetic and thermodynamic studies," *Arabian Journal of Chemistry*, vol. 13, no. 8, pp. 6730–6740, 2020.

[53] S. Baruah, M. Najam Khan, and J. Dutta, "Perspectives and applications of nanotechnology in water treatment," *Environmental Chemistry Letters*, vol. 14, no. 1, pp. 1–14, 2016.

[54] A. L. Ahmad, C. Y. Chan, S. R. Abd Shukor, and M. D. Mashitah, "Adsorption kinetics and thermodynamics of β-carotene on silica-based adsorbent," *Chemical Engineering Journal*, vol. 148, no. 2-3, pp. 378–384, 2009.

[55] E. des Ligneris, L. Dumée, and L. Kong, "Nanofiber-based materials for persistent organic pollutants in water remediation by adsorption," *Applied Sciences*, vol. 8, no. 2, p. 166, 2018.

[56] H. Mazaheri, M. Ghaedi, A. Asfaram, and S. Hajati, "Performance of CuS nanoparticle loaded on activated carbon in the adsorption of methylene blue and bromophenol blue dyes

in binary aqueous solutions: using ultrasound power and optimization by central composite design," *Journal of Molecular Liquids*, vol. 219, pp. 667–676, 2016.

[57] M. Vinayagam, S. Ramachandran, V. Ramya, and A. Sivasamy, "Photocatalytic degradation of orange G dye using ZnO/biomass activated carbon nanocomposite," *Journal of Environmental Chemical Engineering*, vol. 6, no. 3, pp. 3726–3734, 2018.

[58] P. S. Pamidimukkala and H. Soni, "Efficient removal of organic pollutants with activated carbon derived from palm shell: spectroscopic characterisation and experimental optimisation," *Journal of Environmental Chemical Engineering*, vol. 6, no. 2, pp. 3135–3149, 2018.

[59] S. Liu, W.-H. Xu, Y.-G. Liu et al., "Facile synthesis of Cu(II) impregnated biochar with enhanced adsorption activity for the removal of doxycycline hydrochloride from water," *The Science of the Total Environment*, vol. 592, pp. 546–553, 2017.

[60] S. Jemutai-Kimosop, F. Orata, V. O. Shikuku, V. A. Okello, and Z. M. Getenga, "Insights on adsorption of carbamazepine onto iron oxide modified diatomaceous earth: kinetics, isotherms, thermodynamics, and mechanisms," *Environmental Research*, vol. 180, Article ID 108898, 2020.

[61] A. Gebrekidan, M. Teferi, T. Asmelash et al., "Acacia etbaica as a potential low-cost adsorbent for removal of organochlorine pesticides from water," *Journal of Water Resource and Protection*, vol. 7, no. 3, pp. 278–291, 2015.

[62] J. Lan, Y. Cheng, and Z. Zhao, "Effective organochlorine pesticides removal from aqueous systems by magnetic nanospheres coated with polystyrene," *Journal of Wuhan University of Technology-Materials Science Edition*, vol. 29, no. 1, pp. 168–173, 2014.